Lucchi, R.G., St. John, K.E.K., Ronge, T.A., and the Expedition 403 Scientists
*Proceedings of the International Ocean Discovery Program* Volume 403
publications.iodp.org

# Data report: X-ray fluorescence scanning of sediment cores from Site U1618, IODP Expedition 403, Eastern Fram Strait Paleo-Archive[1]

Olga Libman-Roshal,[2a] Lucinda C. Duxbury,[2a] A. Catalina Gebhardt,[2] Alba Gonzalez-Lanchas,[2] Aruggoda K. Isuri U. Kapuge,[2] Lindsey Rose Monito,[2] Lauren Haygood,[2] Gryphen Goss,[2] Jesse Yeon,[3] Brendan Thomas Reilly,[2] Kristen E.K. St. John,[2] Renata G. Lucchi,[2] Thomas A. Ronge,[2] Adriane R. Lam,[2] Brancen Redman,[4] Larry St. John,[5] Maria A. Bárcena,[2] Stijn De Schepper,[2] Nicole M. Greco,[2] Jens Gruetzner,[2] Katrine Husum,[2] Mutsumi Iizuka,[2] Yanguang Liu,[2] Yair Rosenthal,[2] Yuhi Sakai,[2] Yusuke Suganuma,[2] Adukkam Veedu Sijinkumar,[2] and Yi Zhong[2]

[1] Libman-Roshal, O., Duxbury, L.C., Gebhardt, A.C., Gonzalez-Lanchas, A., Kapuge, A.K.I.U., Monito, L.R., Haygood, L., Goss, G., Yeon, J., Reilly, B.T., St. John, K.E.K., Lucchi, R.G., Ronge, T.A., Lam, A.R., Redman, B., St. John, L., Bárcena, M.A., De Schepper, S., Greco, N.M., Gruetzner, J., Husum, K., Iizuka, M., Liu, Y., Rosenthal, Y., Sakai, Y., Suganuma, Y., Sijinkumar, A.V., and Zhong, Y., 2026. Data report: X-ray fluorescence scanning of sediment cores from Site U1618, IODP Expedition 403, Eastern Fram Strait Paleo-Archive. In Lucchi, R.G., St. John, K.E.K., Ronge, T.A., and the Expedition 403 Scientists, Eastern Fram Strait Paleo-Archive. Proceedings of the International Ocean Discovery Program, 403: College Station, TX (International Ocean Discovery Program). https://doi.org/10.14379/iodp.proc.403.202.2026
[2] **Expedition 403 Scientists' affiliations.** Correspondence author: **libmanroshao@montclair.edu**
[2a] Authors contributed equally to this report.
[3] Gulf Coast Repository, Texas A&M University, USA.
[4] Boone Pickens School of Geology, Oklahoma State University, USA.
[5] Department of Physics, University of Virginia, USA.

**Contents**
1 Abstract
1 Introduction
3 Methods and materials
4 Results
7 Data availability
8 Acknowledgments
8 References

**Keywords**
International Ocean Discovery Program, IODP, *JOIDES Resolution*, Expedition 403, Eastern Fram Strait Paleo-Archive, Site U1618, Arctic, West Spitsbergen Current, geochemistry, X-ray fluorescence, XRF, Vestnesa Ridge, Quaternary, paleoclimate

**References (RIS)**

**MS 403-202**
Received 20 January 2026
Accepted 6 April 2026
Published 12 June 2026

## Abstract

High-resolution sediment records from the climatically sensitive Svalbard margin are crucial for reconstructing ice sheet dynamics and ocean–ice sheet interactions during past warm periods. In the boreal summer of 2024, International Ocean Discovery Program (IODP) Expedition 403 collected new sedimentary records from the eastern Fram Strait. Here, we present X-ray fluorescence (XRF) scanning data for the uppermost ~85 m at Site U1618, which was drilled on the eastern Vestnesa Ridge near the continental margin of Svalbard. XRF data, complemented by shipboard magnetic susceptibility and natural gamma radiation records, are used here to improve our understanding of sediment geochemical variability and evaluate stratigraphic variations in elements widely used in proxies of marine productivity, terrigenous sediment input, and authigenic alteration.

## 1. Introduction

The Fram Strait, located between Greenland and Svalbard, is a gateway between the Arctic and North Atlantic Oceans. As the only deep water (~2600 m) passageway connecting the Arctic with global circulation, it plays a key role in regulating the Earth's climate. The north-flowing West Spitsbergen Current (WSC) transports warm, saline North Atlantic Water (NAW) along the western margin of Svalbard, delivering heat to the Arctic, modulating sea ice melt, and shaping circum-Arctic climate. Freshwater input to the North Atlantic during warmer climate intervals reduces surface water density and can weaken the Atlantic Meridional Overturning Circulation (AMOC) (Rahmstorf et al., 2015; Turney et al., 2020). Such AMOC perturbations can accelerate ice sheet retreat in the Southern Hemisphere and drive shifts in global climate patterns (Barker et al., 2009). However, the behavior of the ocean–cryosphere system during past periods of high insolation and/or elevated atmospheric $CO_2$ remains poorly constrained. Addressing this knowledge gap requires studying high-resolution sedimentary records obtained through offshore drilling along

the pathway of NAW inflow. Such sedimentary records were collected during International Ocean Discovery Program (IODP) Expedition 403, Eastern Fram Strait Paleo-Archive, conducted from 4 June to 2 August 2024. Here, we present the X-ray fluorescence (XRF) data completed as part of the IODP programmatic scanning from Expedition 403 Site U1618 on the east terminus of Vestnesa Ridge (Figure **F1**).

The Vestnesa Ridge is an east–west trending sediment drift on Svalbard's western margin that is shaped by the WSC (Eiken and Hinz, 1993) and reflects the region's tectonic, sedimentary, and climatic history. The Svalbard continental margin sedimentary record preserves diverse glaciogenic and bottom current facies, including ice rafting, glacial debris flows, and meltwater plumes (Caricchi et al., 2019; Lucchi et al., 2013, 2015), whereas gas hydrates and associated fluid migration further influence the sedimentary record at Vestnesa Ridge (Himmler et al., 2019; Rasmussen and Nielsen, 2024; Pape et al., 2020; Plaza-Faverola et al., 2023). Site U1618 is located at 78.948°N, 7.475°E on the east terminus of Vestnesa Ridge in close proximity to the continental margin (Figure **F1**), and it is well suited for studies of past ocean–ice sheet interactions, paleo–ice sheet dynamics, WSC variability, ice coverage, effects of climate on past marine biodiversity, and geochemical fluxes (Lucchi et al., 2024; **St. John et al.**, 2026). Three holes were drilled at Site U1618 at a water depth between 1195 and 1196 m. To express core depth, two IODP depth scales are used: core depth below seafloor, Method A (CSF-A), and core composite depth below seafloor, Method A (CCSF-A). The CSF-A depth scale is used for individual holes and is reported as meters below seafloor (mbsf) following Expedition 403 convention (**St. John et al.**, 2026), and the CCSF-A depth scale is used when aligning multiple holes onto a common depth framework. Hole U1618A was drilled to 276.9 mbsf, Hole U1618B was drilled to 414.3 mbsf, and Hole U1618C was drilled to 413.1 mbsf. During programmatic XRF scanning, only Holes U1618A and U1618C were analyzed to ~85 mbsf, corresponding to ~0.711 Ma. This age is interpolated between 0 Ma and paleomagnetic datum of 0.733 Ma at 90.915 mbsf, based on the preliminary shipboard age-depth model (**St. John et al.**, 2026). Although three lithostratigraphic units were defined for Site U1618, the programmatic XRF scanning focused on Subunit IA and the uppermost ~25 m of Subunit IB. Unit I is

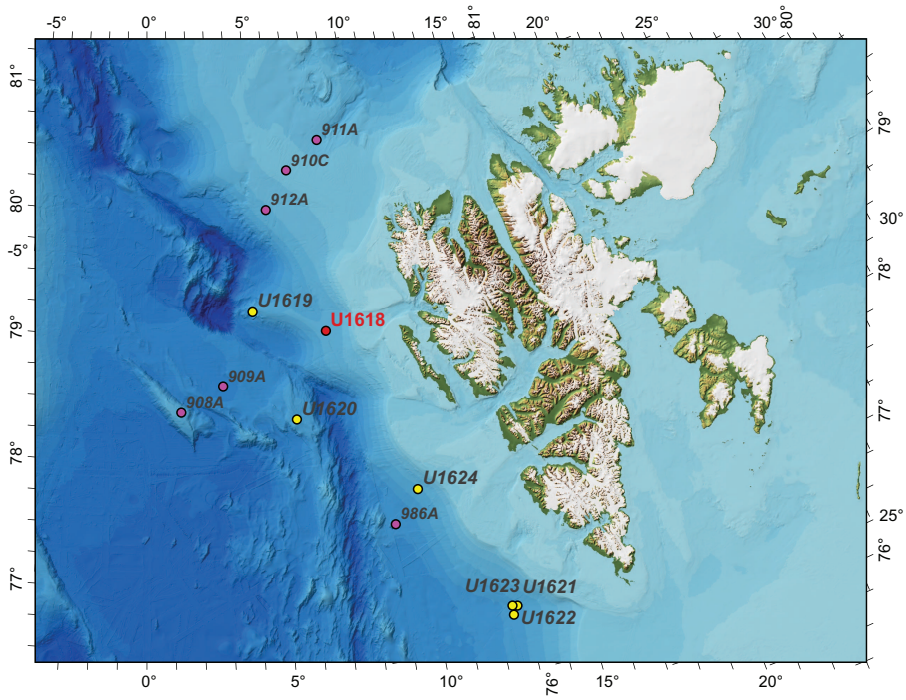


**Figure F1.** Map of study area showing Svalbard (Spitsbergen) Archipelago and surrounding ocean bathymetry, Site U1618. Sites U1618 and U1619 are on Vestnesa Ridge, northernmost Expedition 403 sector. Site U1618 is on eastern terminus of Vestnesa Ridge, ~22 km from shelf edge of Kongsfjorden glacial trough in northwestern Spitsbergen. Red = Site U1618, yellow = other Expedition 403 sites (St. John et al., 2026), pink = Ocean Drilling Program Leg 151 sites (Myhre, Thiede, Firth, et al., 1995).

characterized by soft to firm silty clay with intervals of coarser clayey silt/sandy mud and occasional clasts and gravel that occurs primarily in the upper part of the unit. This unit generally shows little evidence of diagenetic overprinting, which is a concern in the lower (older) lithostratigraphic units at this site. Unit I is separated into Subunits IA and IB. Subunit IA is the youngest in the sequence and has soft "soupy" (Jutzeler et al., 2025) sediments, especially in the uppermost cores, having less bioturbation and a greater abundance of sand and clasts compared to Subunit IB. Subunit IB is generally more bioturbated, and the sediment is more consolidated compared to Subunit IA (**St. John et al.**, 2026). The XRF data set presented here includes low-resolution (5 cm step) scans extending from the seafloor into the uppermost part of Subunit IB and selected sections measured at high resolution (2 mm step), which are limited to the upper portion of Subunit IA. Complementary XRF data sets have been generated for other Expedition 403 sites, including Site U1619 (in prep.), Site U1620 (in prep.), Site U1623 (**Gonzalez-Lanchas et al.**, 2026), and Site U1624 (in prep.).

# 2. Methods and materials

Site U1618 XRF scans were completed postcruise in the boreal fall of 2024 using the fourth generation Avaatech XRF core scanner (XRF2) at the IODP Gulf Coast Repository in College Station, Texas (USA). The instrument is equipped with a water-cooled 100 W rhodium side-window X-ray tube, a Brightspec SiriusSD silicon drift detector, and a Topaz-X high-resolution digital multichannel analyzer. Records for downcore elemental abundance were obtained for select elements from Mg ($Z$ = 12) through Mo ($Z$ = 42) at sampling intervals of approximately 5 cm for low-resolution scans and 2 mm for high-resolution scans, using excitation energies of 10 and 30 kV. A 10 kV setting (6 s exposure time for low-resolution scans; 20–34 s for high-resolution scans) with no filter was used to detect major and minor elements including aluminum (Al), silicon (Si), potassium (K), calcium (Ca), titanium (Ti), manganese (Mn), iron (Fe), chromium (Cr), phosphorus (P), sulfur (S), and magnesium (Mg). The 30 kV setting (6 s exposure for low-resolution scans; 20–34 s for high-resolution scans) with a thick Pd filter was used to detect heavier elements, including iron (Fe), nickel (Ni), strontium (Sr), rubidium (Rb), bromine (Br), zirconium (Zr), and zinc (Zn).

## 2.1. Core preparation

Archive-half sections were first allowed to reach room temperature. Then, the surface of each archive-half-section was gently scraped with a glass slide to level the material and expose a fresh face for scanning. The scraping was performed parallel to the bedding plane to avoid stratigraphically disturbing the sediment. The glass slide was cleaned between scrapes to avoid cross-contamination. For soupy intervals, Kimwipes were used to absorb excess water, and surfaces were subsequently flattened with a glass slide. After leveling the core surface, a 4 µm Ultralene film was placed over the core and secured to the liner with tape. Ultralene film was used to protect the detector and prevent contamination during downcore measurements.

## 2.2. Sample selection

Low-resolution scanning was conducted at nominal 5 cm intervals, with spacing manually adjusted as needed to exclude disturbances. Measurement points were placed only in visually undisturbed intervals of the core, avoiding air-filled cracks, large dropstones or ice rafted debris, and any disturbed sediment features. Scanned intervals were between 4.974 and 85.946 m CCSF-A (splice depth), equivalent to 4.95–83.66 mbsf, for Hole U1618A and between 0.344 and 60.347 m CCSF-A, equivalent to 0.07–58.88 mbsf, for Hole U1618C (Figure **F2**). High-resolution scanning was conducted on sections selected to correspond with complementary analyses underway (e.g., sections sampled for sedimentary ancient DNA analyses). High-resolution XRF measurements were acquired at 2 mm steps for Hole U1618A intervals 4.926–10.858 m CCSF-A (4.902–10.834 mbsf), 16.907–18.333 m CCSF-A (16.300–17.726 mbsf), and 24.710–29.170 m CCSF-A (23.940–28.400 mbsf) and Hole U1618C intervals 0.281–1.725 m CCSF-A (0.002–1.446 mbsf), 9.311–16.265 m CCSF-A (8.776–15.730 mbsf), 17.454–24.822 m CCSF-A (16.802–24.170 mbsf), and 28.154–32.602 m CCSF-A (27.782–32.230 mbsf) (Figure **F2**).

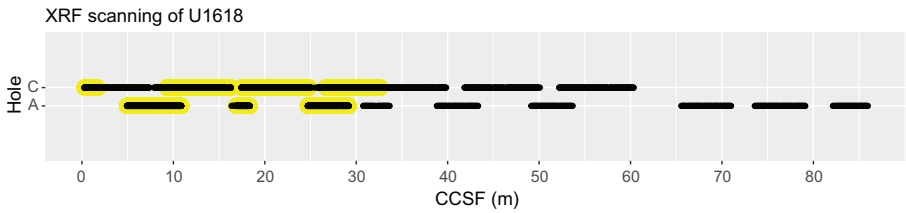


**Figure F2.** Programmatic XRF scanning coverage, Site U1618. Black = low-resolution scanning, yellow = high-resolution scanning.

## 2.3. Quality control

To maintain consistent data quality during XRF core scanning, laboratory standards were analyzed at the start and end of each scanning day using the same excitation settings as the core samples. These measurements were used to track instrument stability and detect any potential calibration drift over time. A continuous helium flow was maintained throughout scanning to minimize atmospheric interference, improve signal stability, and reduce background noise from ambient air.

Raw spectral data were processed into elemental peak areas and exported as count data using the Brightspec XRF spectral processing software bAxil. Data quality control was applied separately for low- and high-resolution data sets. For low-resolution scans, samples with throughput values below 150,000 counts/s were excluded because such values may indicate that the detector window did not fully contact the sample surface or landed on a void. Samples with positive argon (Ar) counts were also removed because they indicate detection of ambient air due to incomplete contact with the sample surface. For high-resolution data, only Ar-based filtering was applied because the counts per second cutoff is not calibrated to the smaller scanning window. Quality control based on throughput and Ar values was implemented in R, modified from the code created by Robustelli Test and Koorapati (**https://github.com/Ravikiran2316/IODP-Exp.-390-393-XRF**) for the IODP Expedition 390/393 XRF data (Lam et al., 2024).

A quality-controlled version of the Site U1618 programmatic XRF data set is available on PANGAEA (Libman-Roshal et al., 2026a, 2026b). The raw XRF data archived in the Laboratory Information Management System (LIMS) database have not been quality checked and may contain values unsuitable for interpretation. Users should therefore exercise caution when using the LIMS data set directly.

## 2.4. Magnetic susceptibility and natural gamma radiation

XRF data are integrated with two Site U1618 physical properties measured on the R/V *JOIDES Resolution* during Expedition 403: magnetic susceptibility (MS) and natural gamma radiation (NGR) (**St. John et al.**, 2026). MS is a dimensionless parameter that indicates how much a material is magnetized by an external magnetic field. MS was measured at 2.5 cm intervals on whole-round core sections, using a Bartington MS2C loop sensor mounted on the Whole Round Multisensor Logger (WRMSL). NGR was measured at 10 cm intervals on whole-round core sections using the Natural Gamma Radiation Logger (NGRL). The instrument detects gamma rays emitted naturally from the decay of uranium-238 ($^{238}$U), thorium-232 ($^{232}$Th), and potassium-40 ($^{40}$K), with elevated counts typically indicating fine-grained, K-rich layers containing U and Th (**St. John et al.**, 2026).

# 3. Results

## 3.1. Correlation between elements

Correlations among elements from low-resolution XRF count data are shown in Figure **F3**. Strong positive correlations are observed between terrigenous, rock-forming elements such as Al, Ti, and K, which as a group are negatively correlated with biogenic indicator elements such as Ca and Sr.

Br, which is commonly used as a proxy for organic matter, shows no positive correlation with Ca or Sr but instead correlates positively with Rb and Ni, likely reflecting diagenetic effects on Ca and Sr consistent with the sparse biogenic carbonate (foraminifer and nannofossil) record (**St. John et al.**, 2026). Zr behaves independently from the typical detrital components and shows no statistically significant correlations with any of the rock forming elements such as Al, Si, and Ti. Depositional sorting may decouple coarser grains of zircon (where Zr is hosted) from the finer rock-forming minerals. Also notable is the strong negative correlation of Zr with both Fe and Rb. Fe shows a positive correlation with Al and Ti, suggesting Fe coupling with terrigenous components, consistent with limited mobilization of Fe into authigenic phases in the uppermost ~85 m of the Site U1618 record. The strongest positive correlations of the record are between Al and Si ($\rho$ = 0.87, p-value = 0.00E+0), Fe and Co ($\rho$ = 0.92, p-value = 0.00E+0), and Rb and K ($\rho$ = 0.83, p-value = 0.00E+0). The strongest negative correlation is between Rb and Zr ($\rho$ = −0.58, p-value = 1.61E−153). Spearman $\rho$ and corresponding p-values for elemental correlations are reported in PANGAEA (Libman-Roshal et al., 2026c).

## 3.2. Stratigraphic trends

Low-resolution stratigraphic profiles of selected elements (Al, Si, Rb, Ca, S, Fe, Zr, and Br) were generated across the uppermost ~85 meters composite depth (mcd) of the sedimentary record (Figure **F4**) to examine compositional trends and environmental shifts. These elements were chosen because they underpin elemental ratios widely used to distinguish terrigenous versus biogenic inputs and to infer redox conditions and mean grain size. The Ca/Ti ratio is commonly used to

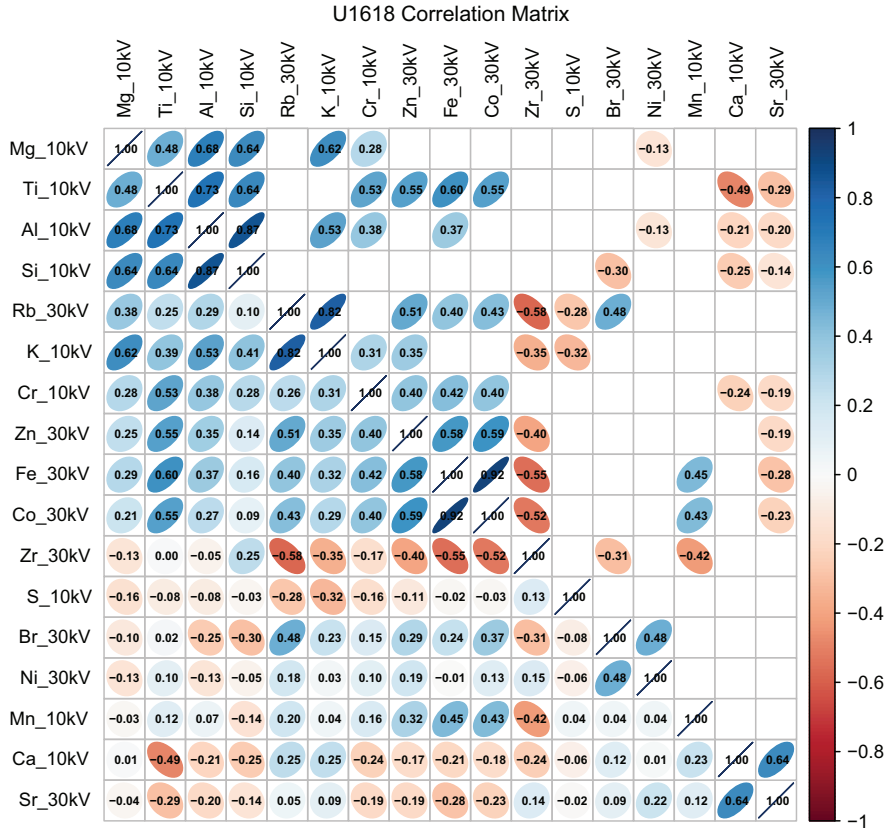


**Figure F3.** Correlation matrix between elements (Mg, Ti, Al, Si, Rb, K, Cr, Zn, Fe, Co, Zr, S, Ni, Mn, Ca, and Sr) measured at low resolution, Site U1618. Lower left triangle is representation of complete correlation between elements; upper right triangle is representation of only statistically significant correlations with p-values < 0.05. Correlations with p-values > 0.05 are left blank in upper triangle. Correlation is represented on color gradient from intense blue (positive correlation; Spearman $\rho$ = 1) to intense red (negative correlation; Spearman $\rho$ = −1). Lighter blue and red indicate weak positive and negative correlations, respectively.

reconstruct changes in surface biogenic production (Ingram et al., 2010; Rothwell and Croudace, 2015), whereas Al/Ti is an indicator of sediment provenance and terrigenous input (Salabarnada et al., 2018). The Si/Ti ratio is used to estimate terrigenous input (e.g., Hanebuth and Henrich, 2009) or biogenic silica (e.g., Agnihotri et al., 2008). Br serves as a proxy for organic matter and marine bioproductivity (Ren et al., 2009; Ziegler et al., 2008) with Rb serving as a lithogenic normalizer in the Br/Rb ratio, and Zr/Rb is used as a proxy for grain size (Ronge and Dbritto, 2024). Together, these ratios support applications such as refining lithostratigraphy (Penkrot et al., 2018), interpreting changes in terrigenous supply, biogenic sedimentation (Hanslik et al., 2013), and grain size variations (Dypvik and Harris, 2001). Shipboard MS and NGR data sets are presented alongside the profiles of individual elements (Figure **F4**) and elemental ratios (Figure **F5**) for Holes U1618A and U1618C. Elemental ratios are presented as natural log ratios, as log-ratios derived from XRF intensities are linearly related to log-ratios of absolute concentrations downcore (Weltje and Tjallingii, 2008) and can therefore serve as a baseline for further interpretation. Negative counts are treated as zeros and values with zeros in the denominator are omitted. Readers are encouraged to explore more advanced, context-specific XRF data standardizations.

Across intervals where Holes U1618A and U1618C were scanned at equivalent splice depths, the resulting elemental profiles exhibit similar trends, although offsets exist between Holes U1618A and U1618C. For example, at ~5–10 m CCSF-A in Hole U1618A, Al and Si profiles are lower and the S profile is higher than their counterparts in Hole U1618C. Consequently, Al/Ti, Si/Ti, and Fe/S ratios in Hole U1618A are lower than these elemental ratios in Hole U1618C over the same interval (Figure **F5**), likely resulting from lithologic variability between holes. Overall, the upper ~0–10 m of the record are marked by high Br/Rb and low Al/Ti at the top followed by a gradual decrease in Br/Rb and increase in Al/Ti, matching the gradual increase in NGR downcore to ~10 m CCSF-A as sediments become more consolidated. Lithostratigraphic Subunit IA cannot be fully compared to Subunit IB because XRF scanning was completed across the entire Subunit IA, whereas only the uppermost ~25 m was scanned in Subunit IB. Nevertheless, Fe/S ratios show prominent peaks in Subunit IA reflecting an excess of Fe relative to S. These peaks are entirely absent in Subunit IB, reflecting Fe mobilization into authigenic phases. Deeper than ~40 m CCSF-A, peaks in Fe/Rb ratios correspond with peaks in MS, suggesting a shared control by terrigenous sediment supply. This correspondence supports a terrigenous rather than diagenetic origin of the MS signal in the examined sections.

Both the low- and high-resolution XRF data (Figures **F5**, **F6**, respectively) show that throughout the scanned interval, the Ca/Ti ratio exhibits trends similar to those of Si/Ti ratio. Similarly, Ca/Ti peaks co-occur with peaks in Zr/Rb, a proxy for grain size or sediment provenance, because Zr is

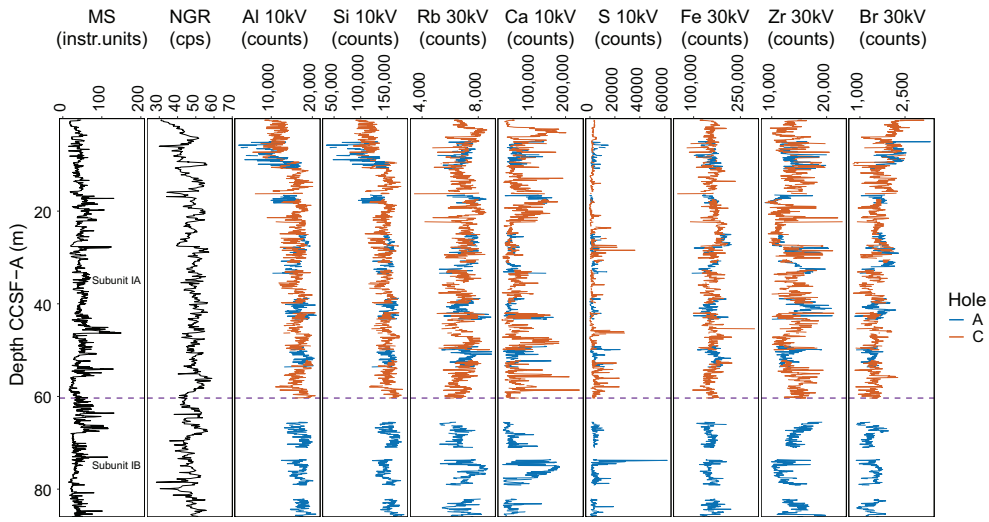


**Figure F4.** MS, NGR, and low-resolution XRF counts for Al, Si, Rb, Ca, S, Fe, Zr, and Br, Site U1618. instr.units = dimensionless instrumental units, cps = counts per second. Dashed line = Subunit IA/IB boundary.

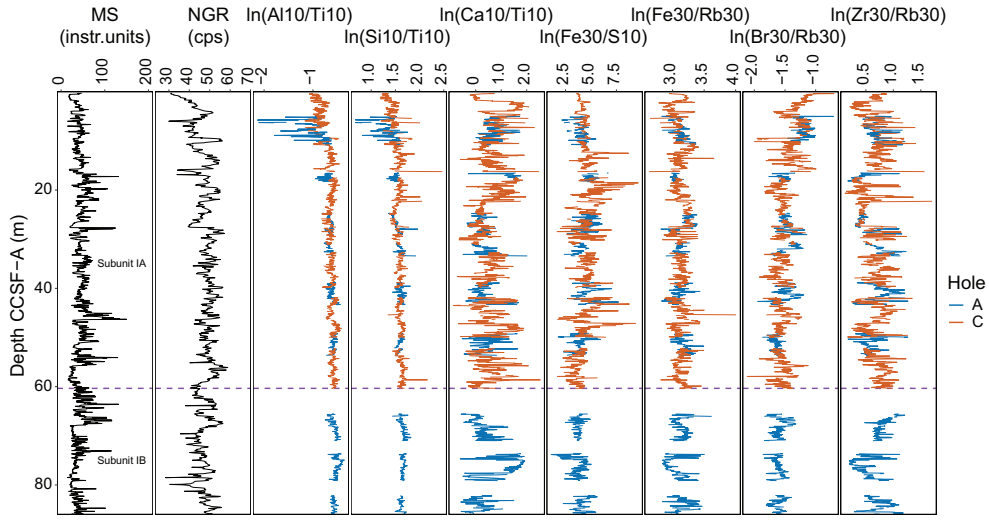


**Figure F5.** MS, NGR, and low-resolution XRF scans, Site U1618. XRF ratios shown as ln ratios: Al/Ti, Si/Ti, Ca/Ti, Fe/S, Fe/Rb, Br/Rb, and Zr/Rb. instr.units = dimensionless instrumental units, cps = counts per second. Dashed line = Subunit IA/IB boundary.

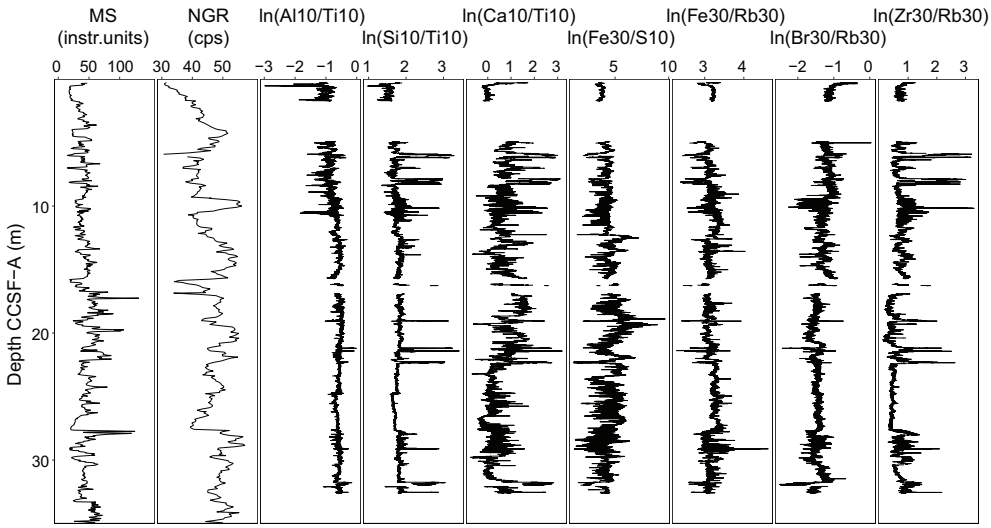


**Figure F6.** MS, NGR, and high-resolution XRF scans (Subunit IA), Hole U1618A. XRF ratios shown as ln ratios: Al/Ti, Si/Ti, Ca/Ti, Fe/S, Fe/Rb, Br/Rb, and Zr/Rb. intr.units = dimensionless instrumental units, cps = counts per second.

common in terrigenous sources and concentrated in coarse, weathering-resistant zircon (e.g., Ronge and Dbritto, 2024; Wu et al., 2020). In contrast, Ca/Ti shows no correspondence with Br/Rb, a proxy for terrestrial vs marine organic input in marine sediments, because Br is enriched in marine organic matter (e.g., Ren et al., 2009; Ziegler et al., 2008) and relatively depleted in terrestrial sources (e.g., Mayer et al., 2007). Together, these observations suggest that the organic component in the uppermost ~85 mcd of the Site U1618 record is largely derived from terrigenous sources rather than from marine productivity.

## 4. Data availability

All raw data are available for download through the IODP LIMS database web portal (**https://iodp.tamu.edu/database**). Processed and quality-controlled data included in this report will be available from the PANGAEA database (Libman-Roshal et al., 2026a, 2026b, 2026c).

## 5. Acknowledgments

This research used samples provided by the International Ocean Discovery Program (IODP). We are grateful to the crew, staff, and technicians on the R/V *JOIDES Resolution* during Expedition 403, as well as the technicians at the Gulf Coast Core Repository at Texas A&M University, College Station, TX (USA), where programmatic XRF scanning was conducted. Expedition 403 and the JRSO were funded by National Science Foundation (NSF) award OCE 1326927. The Expedition 403 programmatic scanning was funded by NSF in agreement with the US Science Support Program (USSSP). Travel funding for US-based scientists participating in XRF scanning was provided by USSSP. Travel funding for the Australian-based scientist was provided by the Australia-New Zealand IODP Consortium (ANZIC).

## References

Agnihotri, R., Altabet, M.A., Herbert, T.D., and Tierney, J.E., 2008. Subdecadally resolved paleoceanography of the Peru margin during the last two millennia. Geochemistry, Geophysics, Geosystems, 9(5). **https://doi.org/10.1029/2007GC001744**

Barker, S., Diz, P., Vautravers, M.J., Pike, J., Knorr, G., Hall, I.R., and Broecker, W.S., 2009. Interhemispheric Atlantic seesaw response during the last deglaciation. Nature, 457(7233):1097–1102. **https://doi.org/10.1038/nature07770**

Caricchi, C., Lucchi, R.G., Sagnotti, L., Macrì, P., Di Roberto, A., Del Carlo, P., Husum, K., Laberg, J.S., and Morigi, C., 2019. A high-resolution geomagnetic relative paleointensity record from the Arctic Ocean deep-water gateway deposits during the last 60 kyr. Geochemistry, Geophysics, Geosystems, 20(5):2355–2377. **https://doi.org/10.1029/2018GC007955**

Dypvik, H., and Harris, N.B., 2001. Geochemical facies analysis of fine-grained siliciclastics using Th/U, Zr/Rb and (Zr+Rb)/Sr ratios. Chemical Geology, 181(1–4):131–146. **https://doi.org/10.1016/S0009-2541(01)00278-9**

Eiken, O., and Hinz, K., 1993. Contourites in the Fram Strait. Sedimentary Geology, 82(1–4):15–32. **https://doi.org/10.1016/0037-0738(93)90110-Q**

Gonzalez-Lanchas, A., Libman-Roshal, O., Duxbury, L.C., Gebhardt, A.C., Kapuge, A.K.I.U., Monito, L.R., Goss, G., Reilly, B.T., Haygood, L., Yeon, J., St. John, K.E.K., Lucchi, R.G., Ronge, T.A., Lam, A.R., Redman, B., St. John, L., Bárcena, M.A., De Schepper, S., Greco, N.M., Gruetzner, J., Husum, K., Iizuka, M., Liu, Y., Rosenthal, Y., Sakai, Y., Suganuma, Y., Sijinkumar, A.V., and Zhong, Y., 2026. Data report: X-ray fluorescence core scanning of IODP Site U1623, Expedition 403, Eastern Fram Strait Paleo-Archive. In Lucchi, R.G., St. John, K.E.K., Ronge, T.A., and the Expedition 403 Scientists, Eastern Fram Strait Paleo-Archive. Proceedings of the International Ocean Discovery Program, 403: College Station, TX (International Ocean Discovery Program). **https://doi.org/10.14379/iodp.proc.403.201.2026**

Hanebuth, T.J.J., and Henrich, R., 2009. Recurrent decadal-scale dust events over Holocene western Africa and their control on canyon turbidite activity (Mauritania). Quaternary Science Reviews, 28(3):261–270. **https://doi.org/10.1016/j.quascirev.2008.09.024**

Hanslik, D., Löwemark, L., and Jakobsson, M., 2013. Biogenic and detrital-rich intervals in central Arctic Ocean cores identified using x-ray fluorescence scanning. Polar Research, 32:18386. **https://doi.org/10.3402/polar.v32i0.18386**

Himmler, T., Sahy, D., Martma, T., Bohrmann, G., Plaza-Faverola, A., Bünz, S., Condon, D.J., Knies, J., and Lepland, A., 2019. A 160,000-year-old history of tectonically controlled methane seepage in the Arctic. Science Advances, 5(8):eaaw1450. **https://doi.org/10.1126/sciadv.aaw1450**

Ingram, W.C., Meyers, S.R., Brunner, C.A., and Martens, C.S., 2010. Late Pleistocene–Holocene sedimentation surrounding an active seafloor gas-hydrate and cold-seep field on the Northern Gulf of Mexico Slope. Marine Geology, 278(1):43–53. **https://doi.org/10.1016/j.margeo.2010.09.002**

Jutzeler, M., Clark, A.S., Manga, M., McIntosh, I., Druitt, T., Kutterolf, S., and Ronge, T.A., 2025. Data report: coring disturbances in advanced piston cores from IODP Expedition 398, Hellenic Arc Volcanic Field. In Druitt, T.H., Kutterolf, S., Ronge, T.A., and the Expedition 398 Scientists, Hellenic Arc Volcanic Field. Proceedings of the International Ocean Discovery Program, 398: College Station, TX (International Ocean Discovery Program). **https://doi.org/10.14379/iodp.proc.398.203.2025**

Lam, A.R., Amadori, C., Borrelli, C., Christeson, G., Estes, E., Guertin, L., Hertzberg, J., Kaplan, M.R., Koorapati, R.K., Lowery, C.M., McIntyre, A., Reece, J.S., Robustelli Test, C., Routledge, C.M., Standring, P., Sylvan, J.B., Thompson, M., Villa, A., Wang, Y., Wee, S.Y., Williams, T., Yeon, J., Teagle, D.A.H., Coggon, R.M., and the Expedition 390/393 Scientists, 2024. Data report: X-ray fluorescence scanning of sediment cores, IODP Expedition 390/393 Site U1583, South Atlantic Transect. In Coggon, R.M., Teagle, D.A.H., Sylvan, J.B., Reece, J., Estes, E.R., Williams, T.J., Christeson, G.L., and the Expedition 390/393 Scientists, South Atlantic Transect. Proceedings of the International Ocean Discovery Program, 390/393: College Station, TX (International Ocean Discovery Program). **https://doi.org/10.14379/iodp.proc.390393.202.2024**

Libman-Roshal, O., Duxbury, L., Gonzalez-Lanchas, A., Gebhardt, A.C., Kappuge, A.K.I.U., Monito, L., Haygood, L., Goss, G., Yeon, J., Reilly, B.T., St. John, K.E.K., Lucchi, R.G., Ronge, T.A., Lam, A.R., Redman, B., St. John, L., Bárcena, M. A., De Schepper, S., Greco, N., Gruetzner, J., Husum, K., Iizuka, M., Liu, Y., Rosenthal, Y., Sakai, Y.,

Suganuma, Y., Sijinkumar, A.V., and Zhong, Y., 2026a. Quality controlled data for the low-resolution scans of IODP Site 403-U1618 [data set]. PANGAEA. **https://doi.org/10.1594/PANGAEA.991434**

Libman-Roshal, O., Duxbury, L., Gonzalez-Lanchas, A., Gebhardt, A.C., Kappuge, A.K.I.U., Monito, L., Haygood, L., Goss, G., Yeon, J., Reilly, B.T., St. John, K.E.K., Lucchi, R.G., Ronge, T.A., Lam, A.R., Redman, B., St. John, L., Bárcena, M. A., De Schepper, S., Greco, N., Gruetzner, J., Husum, K., Iizuka, M., Liu, Y., Rosenthal, Y., Sakai, Y., Suganuma, Y., Sijinkumar, A.V., and Zhong, Y., 2026b. Quality controlled data for the high-resolution scans of IODP Site 403-U1618 [data set]. PANGAEA. **https://doi.org/10.1594/PANGAEA.991432**

Libman-Roshal, O., Duxbury, L., Gonzalez-Lanchas, A., Gebhardt, A.C., Kappuge, A.K.I.U., Monito, L., Haygood, L., Goss, G., Yeon, J., Reilly, B.T., St. John, K.E.K., Lucchi, R.G., Ronge, T.A., Lam, A.R., Redman, B., St. John, L., Bárcena, M. A., De Schepper, S., Greco, N., Gruetzner, J., Husum, K., Iizuka, M., Liu, Y., Rosenthal, Y., Sakai, Y., Suganuma, Y., Sijinkumar, A.V., and Zhong, Y., 2026c. Spearman ρ-values and p-values calculated using R for IODP Site 403-U1618 [data set]. PANGAEA. **https://doi.org/10.1594/PANGAEA.991108**

Lucchi, R.G., Camerlenghi, A., Rebesco, M., Colmenero-Hidalgo, E., Sierro, F.J., Sagnotti, L., Urgeles, R., Melis, R., Morigi, C., Bárcena, M.A., Giorgetti, G., Villa, G., Persico, D., Flores, J.A., Rigual-Hernández, A.S., Pedrosa, M.T., Macri, P., and Caburlotto, A., 2013. Postglacial sedimentary processes on the Storfjorden and Kveithola trough mouth fans: significance of extreme glacimarine sedimentation. Global and Planetary Change, 111:309–326. **https://doi.org/10.1016/j.gloplacha.2013.10.008**

Lucchi, R.G., Sagnotti, L., Camerlenghi, A., Macrì, P., Rebesco, M., Pedrosa, M.T., and Giorgetti, G., 2015. Marine sedimentary record of Meltwater Pulse 1a along the NW Barents Sea continental margin. arktos, 1(1):7. **https://doi.org/10.1007/s41063-015-0008-6**

Lucchi, R.G., St. John, K.E.K., Ronge, T.A., and the Expedition 403 Scientists, 2024. Expedition 403 Preliminary Report: Eastern Fram Strait Paleo-Archive. International Ocean Discovery Program. **https://doi.org/10.14379/iodp.pr.403.2024**

Mayer, L.M., Schick, L.L., Allison, M.A., Ruttenberg, K.C., and Bentley, S.J., 2007. Marine vs. terrigenous organic matter in Louisiana coastal sediments: the uses of bromine:organic carbon ratios. Marine Chemistry, 107(2):244–254. **https://doi.org/10.1016/j.marchem.2007.07.007**

Myhre, A.M., Thiede, J., Firth, J.V., et al., 1995. Proceedings of the Ocean Drilling Program, Initial Reports, 151: College Station, TX (Ocean Drilling Program). **https://doi.org/10.2973/odp.proc.ir.151.1995**

Pape, T., Bünz, S., Hong, W.-L., Torres, M.E., Riedel, M., Panieri, G., Lepland, A., Hsu, C.-W., Wintersteller, P., Wallmann, K., Schmidt, C., Yao, H., and Bohrmann, G., 2020. Origin and transformation of light hydrocarbons ascending at an active pockmark on Vestnesa Ridge, Arctic Ocean. Journal of Geophysical Research: Solid Earth, 125(1):e2018JB016679. **https://doi.org/10.1029/2018JB016679**

Penkrot, M.L., Jaeger, J.M., Cowan, E.A., St-Onge, G., and LeVay, L., 2018. Multivariate modeling of glacimarine lithostratigraphy combining scanning XRF, multisensory core properties, and CT imagery: IODP Site U1419. Geosphere, 14(4):1935–1960. **https://doi.org/10.1130/GES01635.1**

Plaza-Faverola, A., Sultan, N., Lucchi, R.G., El bani Altuna, N., Ramachandran, H., Singhroha, S., Cooke, F., Vadakkepuliyambatta, S., Ezat, M.M., and Rasmussen, T.L., 2023. Spatial changes in gas transport and sediment stiffness influenced by regional stress: observations from piezometer data along Vestnesa Ridge, eastern Fram Strait. Journal of Geophysical Research: Solid Earth, 128(5):e2022JB025868. **https://doi.org/10.1029/2022JB025868**

Rahmstorf, S., Box, J.E., Feulner, G., Mann, M.E., Robinson, A., Rutherford, S., and Schaffernicht, E.J., 2015. Exceptional twentieth-century slowdown in Atlantic Ocean overturning circulation. Nature Climate Change, 5(5):475–480. **https://doi.org/10.1038/nclimate2554**

Rasmussen, T.L., and Nielsen, T., 2024. Glacial-interglacial sedimentation control on gas seepage exemplified by Vestnesa Ridge off NW Svalbard margin. Frontiers in Earth Science, 12:1356341. **https://doi.org/10.3389/feart.2024.1356341**

Ren, J., Jiang, H., Seidenkrantz, M.-S., and Kuijpers, A., 2009. A diatom-based reconstruction of Early Holocene hydrographic and climatic change in a southwest Greenland fjord. Marine Micropaleontology, 70(3):166–176. **https://doi.org/10.1016/j.marmicro.2008.12.003**

Ronge, T.A., and Dbritto, S., 2024. Data report: using XRF scanning–derived grain size analysis for rapid assessment of bottom current velocities on long drill cores from the southern Scotia Sea, IODP Expedition 382. In Weber, M.E., Raymo, M.E., Peck, V.L., Williams, T., and the Expedition 382 Scientists, Iceberg Alley and Subantarctic Ice and Ocean Dynamics. Proceedings of the International Ocean Discovery Program, 382: College Station, TX (International Ocean Discovery Program). **https://doi.org/10.14379/iodp.proc.382.201.2024**

Rothwell, R.G., and Croudace, I.W., 2015. Twenty years of XRF core scanning marine sediments: what do geochemical proxies tell us? In Croudace, I.W., and Rothwell, R.G. (Eds.), Micro-XRF Studies of Sediment Cores: Applications of a non-destructive tool for the environmental sciences. Dordrecht (Springer Netherlands), 25–102. **https://doi.org/10.1007/978-94-017-9849-5_2**

Salabarnada, A., Escutia, C., Röhl, U., Nelson, C.H., McKay, R., Jiménez-Espejo, F.J., Bijl, P.K., Hartman, J.D., Strother, S.L., Salzmann, U., Evangelinos, D., López-Quirós, A., Flores, J.A., Sangiorgi, F., Ikehara, M., and Brinkhuis, H., 2018. Paleoceanography and ice sheet variability offshore Wilkes Land, Antarctica: Part 1. Insights from late Oligocene astronomically paced contourite sedimentation. Climate of the Past, 14(7):991–1014. **https://doi.org/10.5194/cp-14-991-2018**

St. John, K.E.K., Lucchi, R.G., Ronge, T.A., Barcena, M.A., De Schepper, S., Duxbury, L.C., Gebhardt, A.C., Gonzalez-Lanchas, A., Goss, G., Greco, N.M., Gruetzner, J., Haygood, L., Husum, K., Iizuka, M., Kapuge, A.K.I.U., Lam, A.R., Libman-Roshal, O., Liu, Y., Monito, L.R., Reilly, B.T., Rosenthal, Y., Sakai, Y., Sijinkumar, A.V., Suganuma, Y., and Zhong, Y., 2026. Expedition 403 summary. In Lucchi, R.G., St. John, K.E.K., Ronge, T.A., and the Expedition 403 Scientists, Eastern Fram Strait Paleo-Archive. Proceedings of the International Ocean Discovery Program, 403: College Station, TX (International Ocean Discovery Program). **https://doi.org/10.14379/iodp.proc.403.101.2026**

Turney, C.S.M., Fogwill, C.J., Golledge, N.R., McKay, N.P., van Sebille, E., Jones, R.T., Etheridge, D., Rubino, M., Thornton, D.P., Davies, S.M., Ramsey, C.B., Thomas, Z.A., Bird, M.I., Munksgaard, N.C., Kohno, M., Woodward, J., Winter, K., Weyrich, L.S., Rootes, C.M., Millman, H., Albert, P.G., Rivera, A., van Ommen, T., Curran, M., Moy, A., Rahmstorf, S., Kawamura, K., Hillenbrand, C.-D., Weber, M.E., Manning, C.J., Young, J., and Cooper, A., 2020. Early Last Interglacial ocean warming drove substantial ice mass loss from Antarctica. Proceedings of the National Academy of Sciences of the United States of America, 117(8):3996–4006. **https://doi.org/10.1073/pnas.1902469117**

Weltje, G.J., and Tjallingii, R., 2008. Calibration of XRF core scanners for quantitative geochemical logging of sediment cores: theory and application. Earth and Planetary Science Letters, 274(3–4):423–438. **https://doi.org/10.1016/j.epsl.2008.07.054**

Wu, L., Wilson, D.J., Wang, R., Yin, X., Chen, Z., Xiao, W., and Huang, M., 2020. Evaluating Zr/Rb ratio from XRF scanning as an indicator of grain-size variations of glaciomarine sediments in the Southern Ocean. Geochemistry, Geophysics, Geosystems, 21(11):e2020GC009350. **https://doi.org/10.1029/2020GC009350**

Ziegler, M., Jilbert, T., de Lange, G.J., Lourens, L.J., and Reichart, G.-J., 2008. Bromine counts from XRF scanning as an estimate of the marine organic carbon content of sediment cores. Geochemistry, Geophysics, Geosystems, 9(5). **https://doi.org/10.1029/2007GC001932**